



## MXenes stretch hydrogel sensor performance to new limits

Item Type	Article
Authors	Zhang, Yi-Zhou;Lee, Kanghyuck;Anjum, Dalaver H.;Sougrat, Rachid;Jiang, Qiu;Kim, Hyunho;Alshareef, Husam N.
Citation	Zhang Y-Z, Lee KH, Anjum DH, Sougrat R, Jiang Q, et al. (2018) MXenes stretch hydrogel sensor performance to new limits. Science Advances 4: eaat0098. Available: <a href="http://dx.doi.org/10.1126/sciadv.aat0098">http://dx.doi.org/10.1126/sciadv.aat0098</a> .
Eprint version	Publisher's Version/PDF
DOI	<a href="https://doi.org/10.1126/sciadv.aat0098">10.1126/sciadv.aat0098</a>
Publisher	American Association for the Advancement of Science (AAAS)
Journal	Science Advances
Rights	This is an open-access article distributed under the terms of the Creative Commons Attribution-NonCommercial license, which permits use, distribution, and reproduction in any medium, so long as the resultant use is not for commercial advantage and provided the original work is properly cited.
Download date	2024-04-18 16:38:22
Item License	<a href="http://creativecommons.org/licenses/by-nc/4.0/">http://creativecommons.org/licenses/by-nc/4.0/</a>
Link to Item	<a href="http://hdl.handle.net/10754/628444">http://hdl.handle.net/10754/628444</a>

## Supplementary Materials for

### **MXenes stretch hydrogel sensor performance to new limits**

Yi-Zhou Zhang, Kang Hyuck Lee, Dalaver H. Anjum, Rachid Sougrat, Qiu Jiang, Hyunho Kim, Husam N. Alshareef

Published 15 June 2018, *Sci. Adv.* **4**, eaat0098 (2018)

DOI: 10.1126/sciadv.aat0098

#### **The PDF file includes:**

- fig. S1. Characterization of MXene ( $\text{Ti}_3\text{C}_2\text{T}_x$ ) nanosheets.
- fig. S2. Tensile fracture behaviors of pristine hydrogel.
- fig. S3. Schematics of the uniformly dispersed polymer-clay network structure of M-hydrogel.
- fig. S4. Experimental setup for electromechanical responses of M-hydrogel under compression.
- fig. S5. Electromechanical response of M-hydrogel to vertical motion of object on its surface.
- fig. S6. Anisotropic electric response of M-hydrogel to tensile and compressive strain.
- fig. S7. Motion direction sensing comparison between the pristine hydrogel and M-hydrogel.
- fig. S8. Mechanism of the speed-sensitive property of M-hydrogel.
- fig. S9. Handwriting and vocal sensing performances of pristine hydrogel.
- table S1. GF comparison between the M-hydrogel (4.1 wt %)-based sensor and recently reported hydrogel-based sensors.
- References (36, 37)

#### **Other Supplementary Material for this manuscript includes the following:**

(available at [advances.sciencemag.org/cgi/content/full/4/6/eaat0098/DC1](http://advances.sciencemag.org/cgi/content/full/4/6/eaat0098/DC1))

- movie S1 (.avi format). Stretchability and self-healability of M-hydrogel.
- movie S2 (.avi format). Stretchability and self-healability of pristine hydrogel.
- movie S3 (.avi format). Tensile fracture demonstration of M-hydrogel.
- movie S4 (.avi format). Tensile fracture demonstration of pristine hydrogel.

- movie S5 (.avi format). In situ TEM observation with varying tilt angle.
- movie S6 (.avi format). In situ TEM observation with varying depth of focus.

## Supplementary Materials

### Characterization of MXene ( $\text{Ti}_3\text{C}_2$ ) nanosheets

The Raman and XRD spectra were obtained from vacuum-filtrated film of the obtained MXene nanosheets. The Raman spectrum (fig. S1b) exhibits peaks at 202, 586 and 722  $\text{cm}^{-1}$ , corresponding to the  $A_{1g}$  modes of  $\text{Ti}_3\text{C}_2\text{O}_2$ . The peaks at 285 and 629  $\text{cm}^{-1}$  can be assigned to the  $E_g$  of  $\text{Ti}_3\text{C}_2(\text{OH})_2$  and  $E_g$  of  $\text{Ti}_3\text{C}_2\text{F}_2$ , respectively (36). These peaks reveal the presence of -OH, -O and -F functional groups on  $\text{Ti}_3\text{C}_2\text{T}_x$  MXene surface. The broadening feature around 374  $\text{cm}^{-1}$  is difficult to be assigned to specific vibration modes, however it is typical of  $\text{Ti}_3\text{C}_2\text{T}_x$  MXene (36, 37). The XRD pattern presents one major peak at  $\approx 7^\circ$ , which corresponds to the (0002) planes of  $\text{Ti}_3\text{C}_2$  MXene (28).

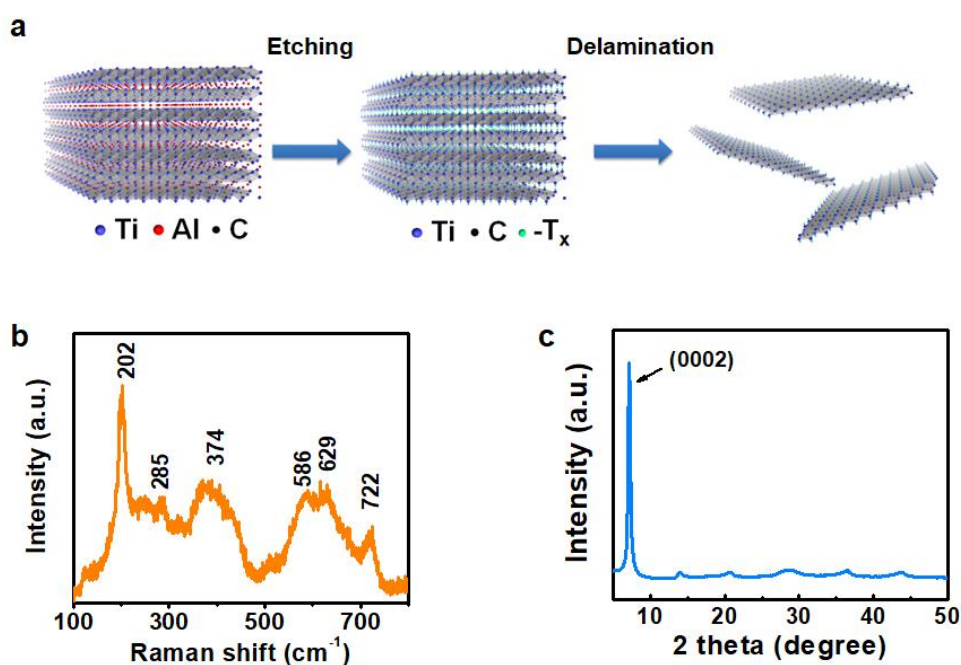


**fig. S1. Characterization of MXene ( $\text{Ti}_3\text{C}_2\text{T}_x$ ) nanosheets.** (a) Schematic for the synthesis of MXene nanosheets; (b) Raman spectrum; and (c) XRD spectrum of MXene film.

### Tensile fracture behavior of pristine hydrogel.

To demonstrate the stretchability of pristine hydrogel, a rectangular piece of pristine hydrogel with a length of 2.5 cm was stretched at a low rate until mechanical failure occurred between 49 cm and 55 cm, which translates to a maximum stretchability of 2,200% (fig. S2a). Two cut pieces form one piece upon gentle touching; however, when stretching,

necking emerges at the contact interface followed by mechanical failure under further stretching (fig. S2b). Clearly, the healability of the pristine hydrogel is inferior to the MXene-modified hydrogel.

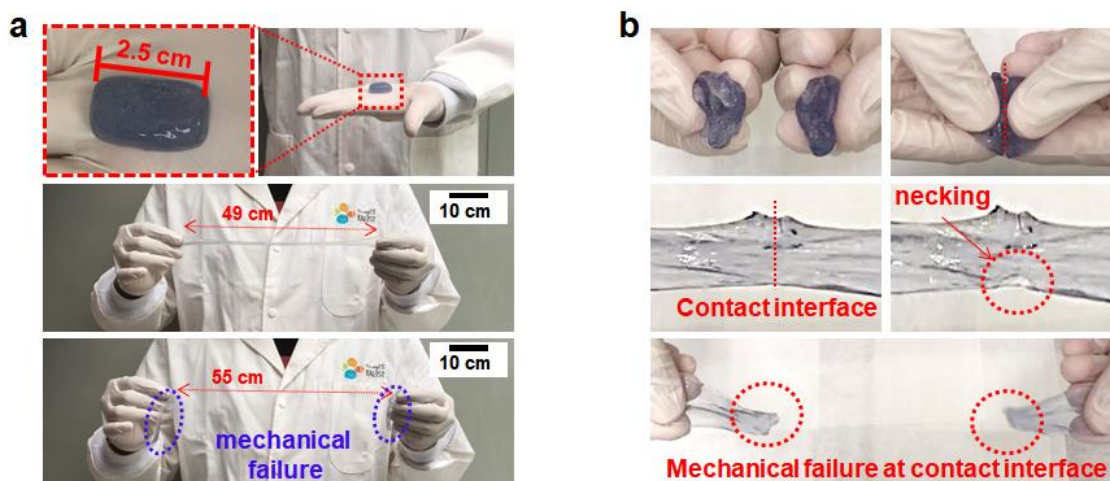


**fig. S2. Tensile fracture behaviors of pristine hydrogel.** (a) Stretchability demonstration of pristine hydrogel; (b) self-healable performance of pristine hydrogel.

Schematics of the uniformly dispersed polymer-clay network structure of M-hydrogel

When MXene nanosheets are added into the PVA hydrogel system, their surface functional groups (-OH, -F, -O, etc.) can create secondary cross-linking (such as hydrogen bonding) with PVA chains and water molecules as shown in fig. S3b. The secondary cross-linking prevents aggregation of the MXene nanosheets through bonding with PVA chains. As a result, the 3D-network structure composed of homogeneously dispersed MXene nanosheets and entangled PVA chains can be formed (fig. S3a).

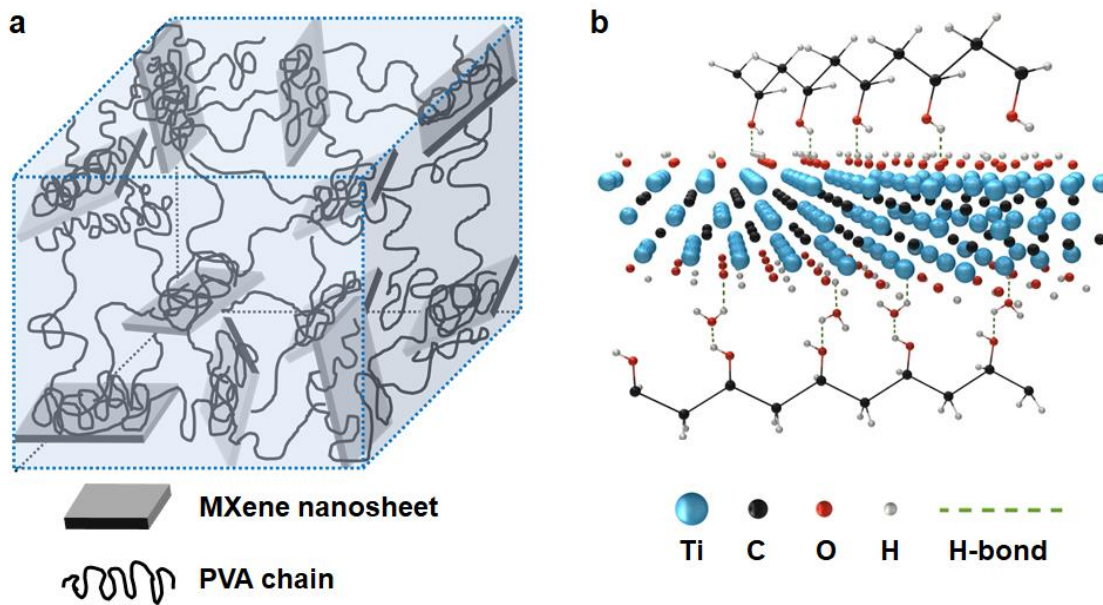


**fig. S3. Schematics of the uniformly dispersed polymer-clay network structure of M-hydrogel.** (a) Uniform distribution of MXene nanosheets within the PVA hydrogel matrix; (b) hydrogen bonds (H-bonds) between PVA chains, water molecules, and MXene nanosheets.

Experimental setup for testing electromechanical responses of M-hydrogel under compression

The syringe filled with M-hydrogel (4.1 wt%) was used for electromechanical compressive tests as shown in the inset of fig. S3. The gauge length and diameter of the M-hydrogel in the syringe were 15 mm and 10 mm, respectively. The resistance of M-hydrogel decreased 60% at a compressive strain of 3%.

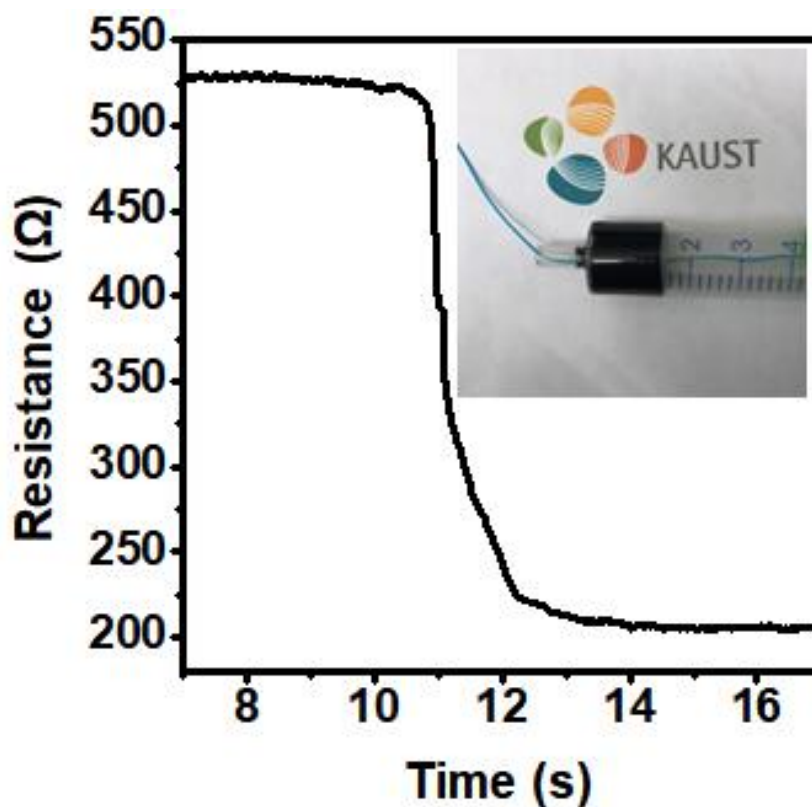


**fig. S4. Experimental setup for electromechanical responses of M-hydrogel under compression.**

### Electromechanical response of M-hydrogel to vertical motion of object on its surface

A model experiment was conducted to demonstrate the viscoelastic property of M-hydrogel. This was accomplished by pushing a round PDMS tip with a 3-mm radius against the M-hydrogel contained in a rigid case (inset of fig. S5c) with the dimensions of 26.4 mm  $\times$  26.4 mm  $\times$  3.1 mm (fig. S5a). As figure S5b indicates, the resistance of M-hydrogel increased when the tip was immersed in M-hydrogel. To test the frequency response of M-hydrogel, the electric responses were measured at the frequencies of 0.1, 0.25, and 1 Hz, with an amplitude of 2 mm (lower schematic fig. S5a). figure S5d presents the corresponding results.

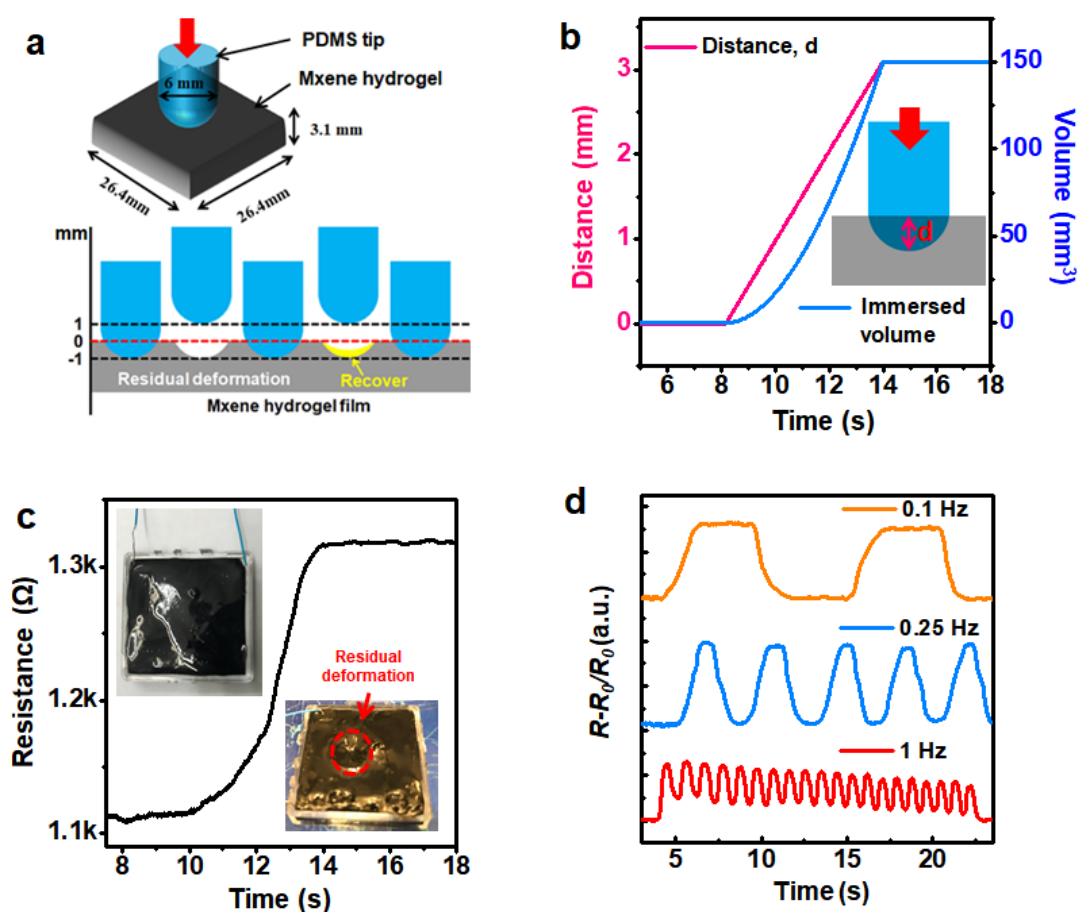


**fig. S5. Electromechanical response of M-hydrogel to vertical motion of object on its surface.** (a) Schematic of experimental set-up; (b) immersed distance of PDMS tip in M-hydrogel (red) and corresponding volume change (blue); (c) resistance change during immersion, inset depicting the residual deformation after the disengagement of the PDMS tip; and (d) electrical response of M-hydrogel to immersion cycles under different motion frequencies.

### Anisotropic electric responses of M-hydrogel to tensile and compressive strain

A model experiment was conducted to explore why motion in the direction of the current can reduce resistance (Fig. 3C). The compressive and the tensile strain were designed to be the same as the copper plate moved, and figure S6a displays the corresponding series circuit. The  $R_{\text{Tens}}$  and  $R_{\text{Comp}}$  represent the resistance of the piece of M-hydrogel under tensile strain and under compressive strain, respectively (both resistances include contact resistance between the copper plate and M-hydrogel). If the sensitivities to tensile and compressive strain were the same, there would be no change in the total resistance because resistance changes in the compressive and tensile regions are the same as the copper plate moves. However, figure S6b demonstrates that the total resistance decreases when the copper plate moves in the current direction; thus, the decrease of  $R_{\text{Comp}}$  is higher than the increase of  $R_{\text{Tens}}$  because of the anisotropic sensitivity to compressive and tensile strains of M-hydrogel.

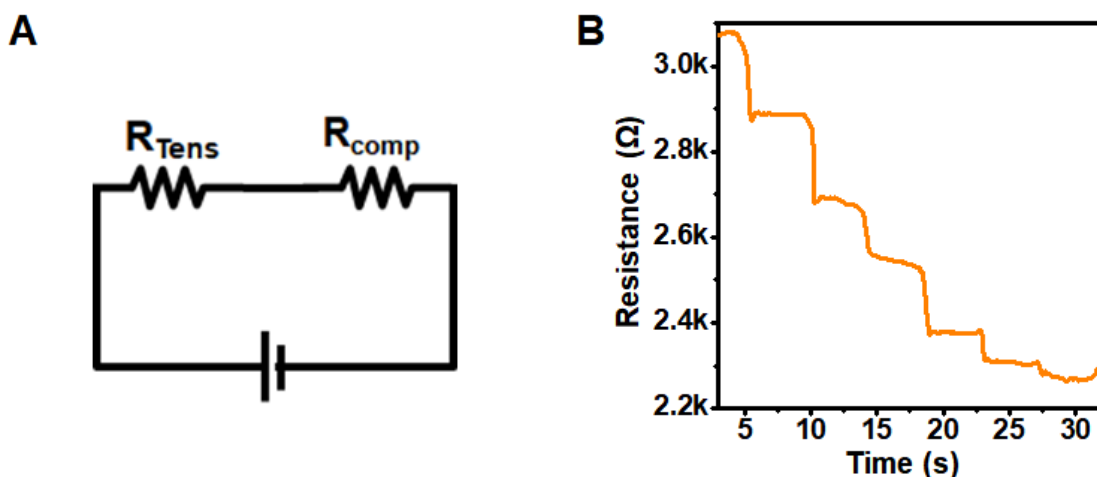


**fig. S6. Anisotropic electric response of M-hydrogel to tensile and compressive strain.** (a) Equivalent circuit and (b) resistance change showing the anisotropic response of M-hydrogel to tensile and compressive strain.

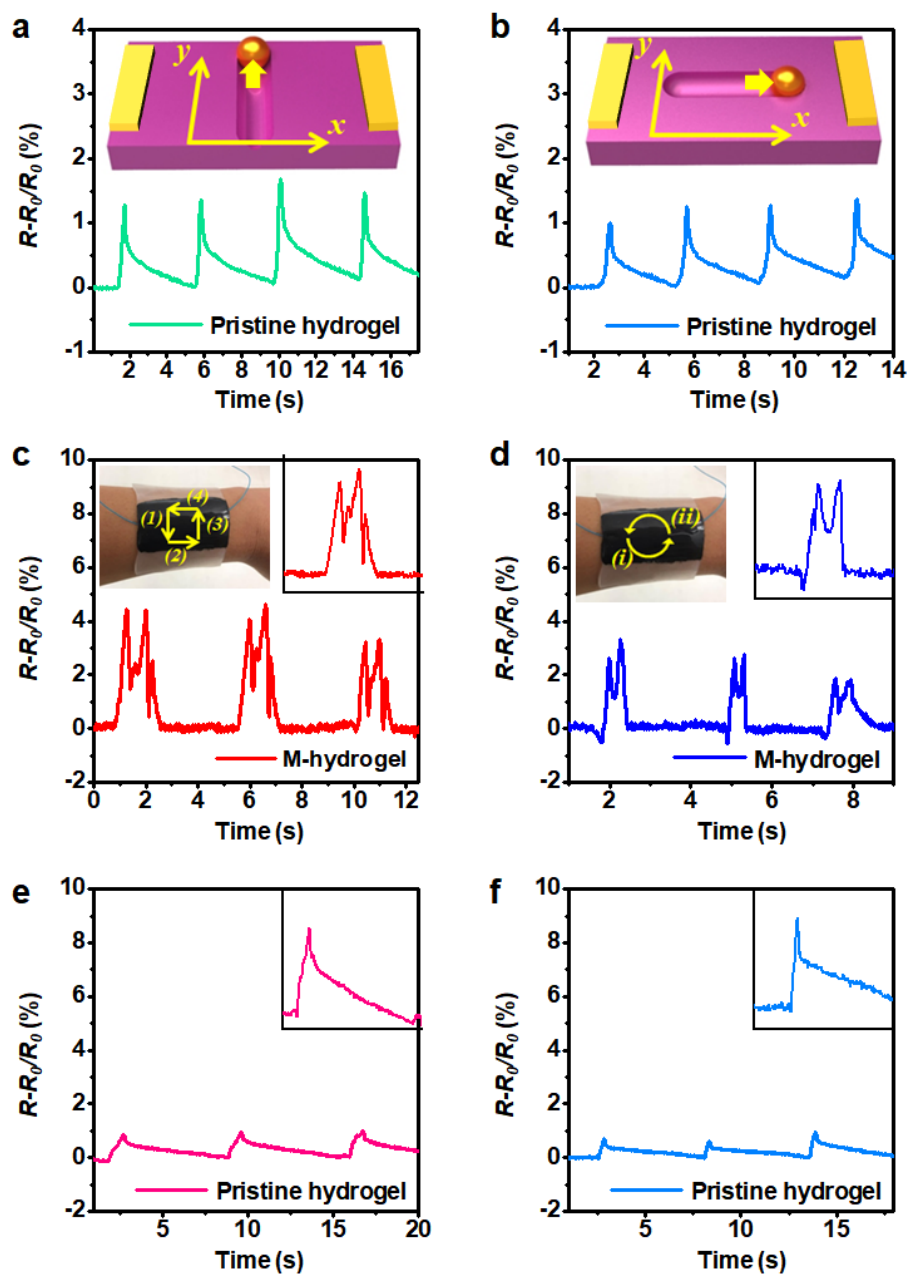


**fig. S7. Motion direction sensing comparison between the pristine hydrogel and M-hydrogel.** Resistance change of pristine hydrogel due to motion on its surface (a) vertical to the current direction and (b) parallel to the current direction. Resistance change of M-hydrogel based E-skin to (c) rectangular and (d) circular motion on its surface. Resistance change of pristine hydrogel based E-skin to (e) rectangular and (f) circular motion on its surface; unlike M-hydrogel, pristine hydrogel cannot detect difference in motion directions and pathways.

### Mechanism of the speed-sensitive property of M-hydrogel

When an object undergoes uniform motion on the M-hydrogel surface, there is no additional deformation (trace) beyond the deformation due to the weight of the object when the speed of motion is lower than the relaxation speed of the M-hydrogel surface (fig. S8a). However, additional traces are uniformly created when the motion velocity surpasses the relaxation speed, which results in larger deformations (fig. S8b).

Furthermore, when the object undergoes uniformly accelerated motion, even larger deformations emerge, as the speed increases after exceeding the relaxation speed of M-hydrogel (fig. 8c). Therefore, in Figure 3F, the downward peaks in region “II” for objects undergoing accelerated motion with higher initial velocity start earlier and have a greater height.

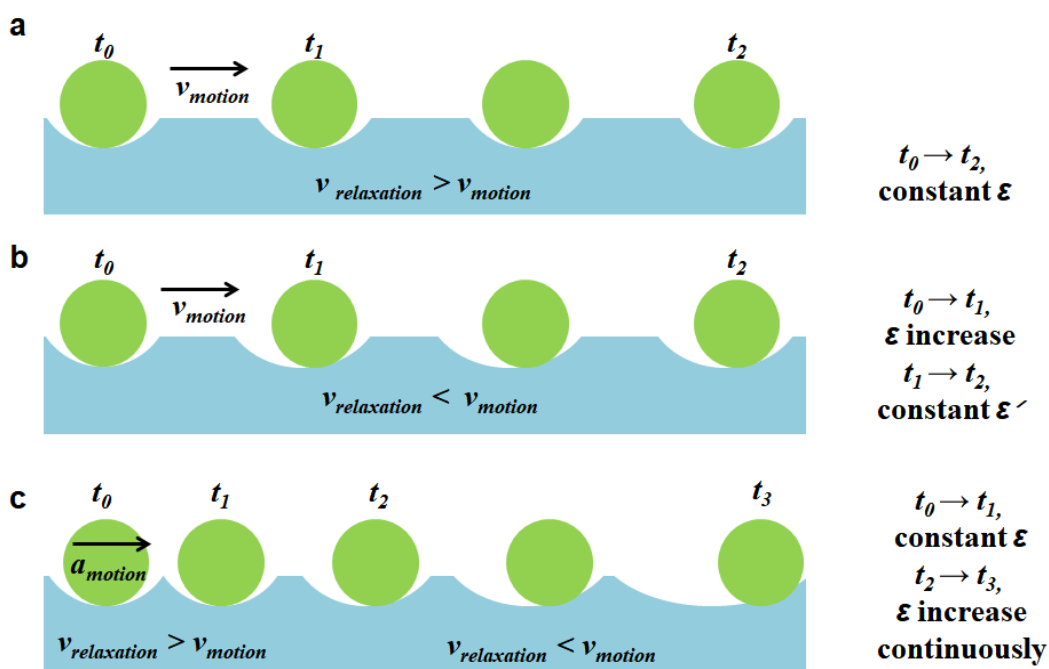


**fig. S8. Mechanism of the speed-sensitive property of M-hydrogel.** including schematics for motion with constant velocity (a) less and (b) greater than the relaxation speed of M-hydrogel and (c) for uniformly accelerated motion.

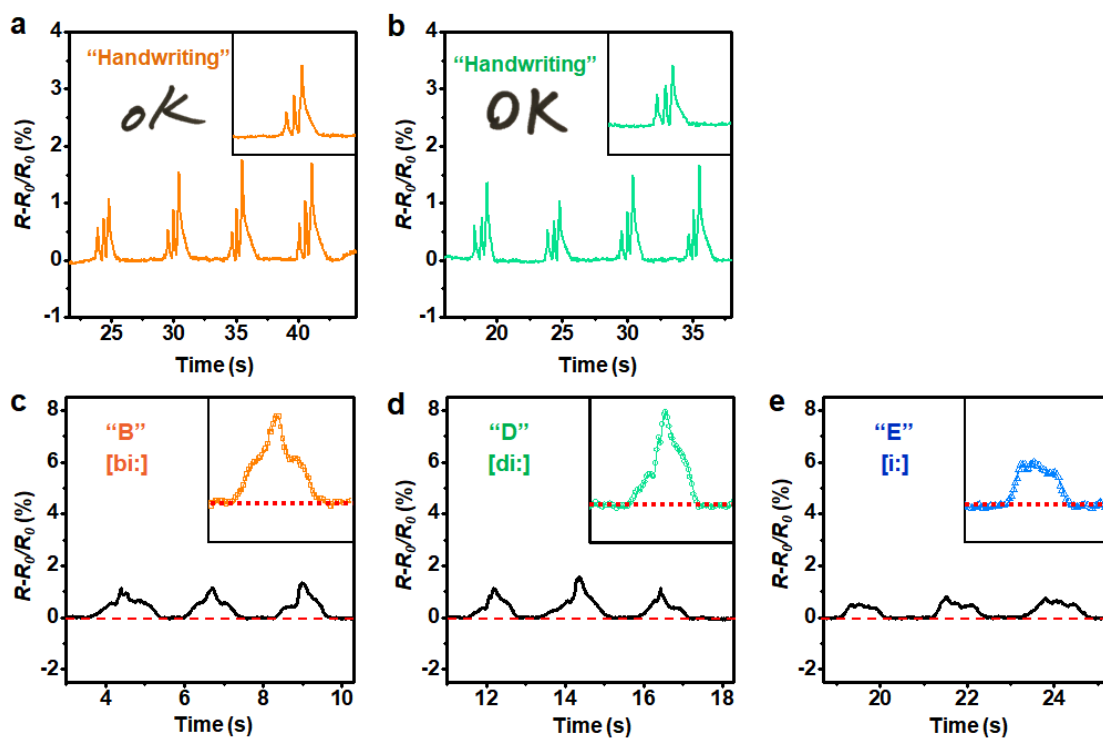


**fig. S9. Handwriting and vocal sensing performances of pristine hydrogel.** (a-b) Resistance change of pristine hydrogel towards “OK” written by two volunteers; unlike M-hydrogel, pristine hydrogel cannot detect different writing styles. Vocal-sensing performance of pristine hydrogel towards similarly sounding letters (c) “B,” (d) “D,” and (e) “E” ; unlike M-hydrogel, pristine hydrogel cannot detect the subtle differences in different syllables.

**table S1. GF comparison between the M-hydrogel (4.1 wt %)-based sensor and recently reported hydrogel-based sensors.**

Base gel	Conductive filler	Gauge factor (tensile strain)	Ref
	SWCNT	1.51 (1000%)	
Poly (vinyl alcohol) (PVA)	Graphene	0.92 (1000%)	31
	Silver nanowire	2.25 (1000%)	
PVA/ Polyvinylpyrrolidone (PVP)	Fe <sup>3+</sup>	0.478 (200%)	29
Polyacrylamide (PAAm)	LiCl	0.84 (40%)	32
PAAm	Graphene	9 (30%)	12
PAAm	K-carrageenan	0.23 (100%)	33
PVA	MXene (Ti <sub>3</sub> C <sub>2</sub> T <sub>x</sub> )	25 (40%)	This work